Supplementary Information

Pencil's Graphite Cores for Pattern Recognition Applications

Caroline Y. N. Nicoliche, Gabriel F. Costa, Angelo L. Gobbi, Flavio M. Shimizu, and Renato S. Lima*

Abstract: Ready-to-use sensing probes have been used to develop a rapid-production, low-cost, fast, and sensitive electronic tongue, which consisted of electric double-layer microfluidic capacitors. Pencil's graphite cores consisting of rough flake-graphite with varied ratios of graphite, clay, and wax assured differential interactions towards pattern recognition applications.

Table of Contents

1. Chemicals and samples

Sodium chloride (NaCl), caffeine, sucrose, and nitric acid (HNO_3) were purchased from Sigma-Aldrich (St Louis, MO), whereas hydrochloric acid (HCl) and potassium chloride (KCl) were acquired from Hexis (Jundiaí, São Paulo, Brazil). Sylgard 184 silicone and AZ® 50XT resist were purchased from Dow Corning (Midland, MI) and Microchemicals (Ulm, Germany), respectively. MWCNTs were supplied from CNT Co. (Incheon, South Korea). Distilled water was obtained with resistivity of 0.48 MΩ cm (Tecnal TE-2755, Piracicaba, Brazil). Five brands of commercial mineral water and tap and filtered water were obtained in Campinas-SP, Brazil.

2. Fabrication of the chip, characterization of the electrodes, and assays

Microfluidic device

As previously described by our group,[1] microfluidic chips composed of a single piece of polydimethylsiloxane (PDMS) were obtained through the bondless and cleanroom-free technique of PSR. It basically requires a laboratory oven and allows the fabrication of dozens to hundreds of chips in 1 h. Briefly, 3D-printed cylinders in poly(lactic acid) (PLA) were used as scaffolds of the electrode channels, whereas the sample channel was defined by a stainless-steel capillary with 700.0-µm diameter. All the scaffolds were supported onto 3D-printed pool-like pieces. From two pieces of 19 mm × 59 mm × 15 mm, 12 chips could be attained in roughly 1 h. Consequently, this technique is scalable for large-scale fabrication. PSR is further a green prototyping since it avoids both the use of solvent and waste production.

Briefly, the scaffold of the electrode channels consisted of 3D-printed cylinders in PLA that were shaped by an extrusion printer of fused deposition modelling (FDM, 3D Sethi3D AiPA3, Campinas, Brazil). Conversely, a stainless-steel capillary with 700.0 µm in diameter defined the sample channel. The 3D-printed pieces were placed on both below and above the sample channel scaffold to form EDL capacitors by reversibly putting the electrodes upon the fabrication of the chip. To prepare PDMS, its monomer and curing agent were mixed at 10:1 w/w ratio and, then degassed under vacuum during 20 min. Before the insertion of the electrode channel scaffolds and pouring of PDMS as illustrated in **Figure S1A**, the photoresist AZ® 50XT was deposited on the stainless-steel capillary (sample channel scaffold) by centrifugation at 2000 rpm for 10 s for three times and dried at room temperature for 20 min. Such resist was intended to avoid the filling of the scaffold junctions by PDMS to warrant the contact between sample and electrode. The channel scaffolds were supported in 3D-printed pool-like pieces of PLA. The PDMS cure was conducted at 60 °C in a laboratory oven (Blue M, Blue Island, IL) for 1 hour and a final hard baking for 30 min in 120 °C. **Figure S1B** shows photos of a device without and with electrodes. Images of the channels were reached by scanning electron microscopy (SEM, FEI Quanta 650 Thermo Scientific, Ashford, UK) and stereoscopy (Leica M125, Wetzlar, Germany). The stereoscopy images were employed to measure the channel and electrode diameters using the software LAS Core V3.8.

Electrodes

The lead pencils are the most widely available hetero-structured graphite that the people worldwide use daily for writing, sketching, and coloring.[2] Herein, a set comprising twelve pencils of different grading scales were acquired from Brevillier Urban & Sachs company (Cretacolor, Hirm, Austria). These cores exhibit characteristic G/C ratios and are frequently utilized for high-quality and artistic writing and drawing. The G/C ratios define the core hardness in accordance with twenty HB scales, 9H up to 9B. As the core becomes softer through the increase in the quantity of graphite (higher G/C ratios as indicated by the B scale; the letter 'B' designates the pencil's mark blackness), it deposits more graphite leaving darker marks onto paper. In contrast, an increase in the amount of clay (lower G/C ratios as indicated by the H scale; the letter 'H' indicates the pencil's core hardness) creates harder cores that leaves lighter marks onto paper. The pencils have distinct chemical compositions, roughnesses, and electric resistivities. In this regard, each graphite core is expected to produce unique capacitance spectra to a same analyte, acting as a sensing probe of the e-tongue as it was indeed observed herein.

The graphite cores were easily removed from the pencils after wetting the wood with water. Nonetheless, only the cores could be obtained as recently provided by Faber Castell company (São Carlos, Brazil) for future investigations. In practice, the pencil's graphite cores were manually inserted in the PDMS channels and, then short-circuited with the aid of copper pieces to create an association of capacitors in parallel. Analyses of electrical resistance, atomic force microscopy (AFM), scanning electronic microscopy (SEM), energy dispersive X-ray spectroscopy (EDS), Raman spectroscopy, thermogravimetric analysis (TGA), and X-ray photoelectron spectroscopy (XPS) of the cores were performed. The electric resistances of the twelve cores were measured by a multimeter of Agilent (34405A Digital Mul-timeter 5 ½

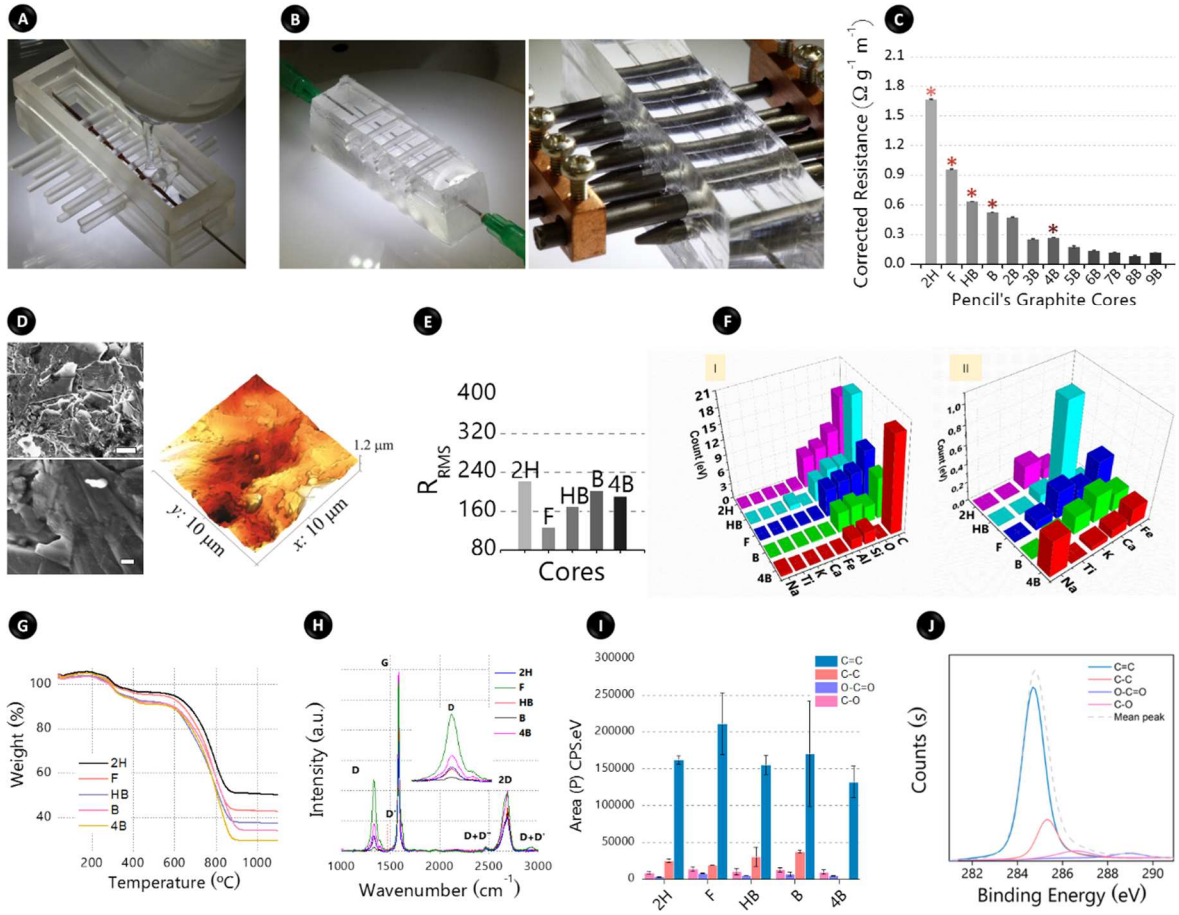

Figure S1. **(A)** Pouring PDMS on the scaffolds for PSR fabrication. **(B)** Device without and with electrodes. Values of **(C)** resistance and **(D)** roughness of the cores. **(E)** Elementary composition of the cores by EDS. **(F)** SEM and AFM images of the B core. **(G)** TGA plots. **(H)** Raman data. **(I)** Amounts of C sp^3 and sp^2 detected by XPS. **(J)** High-resolution C spectrum of the B core by XPS. The scale bars in **(D)** mean 2 µm (top image) and 200 nm (bottom image).

Digit, Santa Clara, CA). The resistances were corrected by the ratio with the mass and length of the cores. Based on the higher differences between these values, five cores were selected for the next analyses. Images of the chosen electrodes were recorded by field emission SEM (FE-SEM, Zeiss Sigma, Jena, Germany) equipped with EDS operating at 3.0 kV and AFM (NX10 Park Systems, Santa Clara, CA). The AFM images to assess topography were attained in the tapping mode at 0.3 Hz using a FMR tip of Nanosensors (Neuchâtel, Switzerland). The electric AFM measurements to record d*C*/d*Z* data were made with Pt/Ir tip (NanoSensor PPP-EFM), nominal resonance of 75 kHz and force constant of 2.8 N m^{-1}. The chemical analyses with Raman spectroscopy were accomplished in the micro-Ra-man spectrometer of LabRam HR Evolution (Horiba, Japan) using laser line of 633 nm, power of 25%, and 600 grooves per mm grating in the range from 200 up to 1600 cm^{-1}. Measurements by XPS were accomplished in the Thermo Fisher Scientific K-Alpha spectrometer (Waltham, MA), whereas the TGA assays were conducted in the NETZSCH TGA/STA 449 F3 Jupiter equipment (Boston, MA) with heating rate of 5 °C min^{-1} at synthetic air atmosphere. As discussed in the main text, the results of the corrected resistances, root mean square roughnesses (R_{RMS}) by AFM, relative compositions of the cores by EDS, SEM and AFM images, plots of TGA and Raman, relative quantities of C sp^3 and sp^2 by XPS and high-resolution C XPS spectrum are shown in **Figure S1C-J**. From elementary composition of the five selected pencil's graphite cores by EDS, C, O, Si, and Al are their major constituents. The elements Fe, Ca, K, Ti, and Na were also detected. The quantities of Si and Al increased with the content of clay as expected and in agreement with investigations addressed in the literature through X-ray fluorescence (XRF).[2] In the latter work, Bhowmik further performed X-ray diffraction (XRD) measurements that confirmed the hexagonal crystalline structure of the pencils 5H, 2H, HB, 2B, and 6B. The decomposition in approximately 270 and 600 °C in the TGA plots are attributed to wax and carbon, respectively. From the Raman data, overtone bands were verified at 2465 (*D*+*D*″), 2685 (*2D* or *G*′), and 2928 cm^{-1} (*D*+*D*′). The resulting I_D/I_G ratios were 0.32 (2H), 0.90 (F), 0.23 (HB), 0.06 (B), and 0.29 (4B).

Analyses

The tests were made at stationary media applying a voltage of 25 mV ac, integration time of 2 s, frequencies from 10^0 to 10^6 Hz, and dc voltages from –1.0 to +1.0 V at room temperature. The two-dimensional PCA method, usually applied in combinatorial systems for discrimination purposes, was used in MATLAB software to project the data in 2D score plots of coordinates called principal components. The pattern recognition ability was quantized by silhouette coefficient (S).[1c] Regarding the differential capacitance (C_d) *vs.* frequency plots, the data are driven by EDL charging at metal-electrolyte interfaces (C_{sol}) in frequencies lower than roughly 10^2 Hz. In the range of roughly

10^2 up to 10^4 Hz, the effect of the electrode material is predominant (C_M), whereas the data are governed by capacitor geometry at greater frequencies. The spectra based on frequency and potential were acquired in one run. The potential-based spectra were attained at 10^0 Hz since the resulting data in this region are governed by C_{Sol}. This feature leads to sensitive measurements to different samples. With the aid of polytetrafluoroethylene (PTFE) luer-lock connectors and Tygon tubes (0.7 mm i.d.), a plastic syringe was used to clean the electrodes and channels between the capacitive measurements with water and ethanol as well as to change the samples. The impedance experiments were conducted at stationary regime.

3. Adsorptions on core/solution interfaces

As described in the main text, the EDL charging can be modelled by an association of C_M and C_{Sol} in series so that:[3]

$$\frac{1}{C_d} = \frac{1}{C_M} + \frac{1}{C_H} + \frac{1}{C_D} \quad (1)$$

The nonspecific adsorptions shown in **Scheme 1** (main text) involve only long-range electrostatic interactions. In these situations, the charge balance is guaranteed by the excess of ions of opposite charge on electrode and deficiency of ions with same charge. Conversely, the specific adsorptions are related to short-range (electrostatic and chemical) effects and lead to the excess of both the ions on EDL to ensure the interface electroneutrality due to the phenomenon of superequivalent adsorption. The latter interactions depend on specie identity and are usually noted only for anions because of their low charge-radius ratio and, then poor hydration sheath. Still in relation to the **Scheme 1**, the electrical circuit is corresponding to ideally polarizable electrodes that are assumed in this work because of the absence of charge transfer reactions as confirmed through cyclic voltammetry (data not shown). In this case, the elements associated with faradaic impedance such as charge-transfer resistance and Warburg impedance are eliminated.

4. Differential interactions afforded by the cores

The differential capacitance, C_d, can be obtained by impedance analyses. For ideally polarizable electrodes, the total impedance of the cell consists of a RC circuit in series. In this case, the impedance (Z) at any dc potential is given by the equation:[4]

$$Z = Z_{Re} + iZ_{Im} = R + (iC_d\omega)^{-1} \quad (2)$$

where i is an imaginary unit, Z_{Re} and Z_{Im} are the real and imaginary parts of the impedance, respectively, and ω is the angular frequency of the ac perturbation. Then, the capacitance can be calculated from the measured impedance values as follows:

$$C_d = -(\omega Z_{Im})^{-1} \quad (3)$$

The existence of differential interactions from the cores was confirmed in tests to individual solutions of HCl and caffeine, both at 0.1 mmol L^{-1}. Frequency-based spectra, electrocapillary and charge (q) curves, and the distinct potentials of zero charge (V_{PZC}) from the probes are illustrated in **Figure S2A-H** as described in the main text. The electrocapillary curves did not follow perfect parables and, therefore a non-linear increase in q with potential was verified in consistence with C_d variations. In relation to the extremes 2H and 4B, HB and B generated the larger absolute values and changes of C_d, which are associated with greater deviations in linearity of the q plots. The absence of any correlation between G/C ratio and response pattern was expected because of the plenty of variables affecting C_d. As discussed in the main text, the discrepancies in PZC also support the different χ_M. This feature is in agreement with the equation:[3a]

$$\mathrm{PZC} = \frac{\Phi_M}{F} + \text{constant} \quad (4)$$

Where Φ_M is the metal work function that is the sum of χ_M and electron chemical potential.

Based on data points related to HCl and caffeine solutions (0.1 mmol L^{-1}) in PCA plots of **Figure S2I**, the single responses recorded by the short-circuited probes led to larger cluster separation when compared with the use of response patterns independently obtained by the five individual cores. This result is because of the detection area that is around five times greater in the case of the experiments with single response. This increase in area improves the sensibility of capacitive sensors by raising the charge accumulated on capacitor plates.[3b]

5. Discrimination of individual solutions

The ability of the single response μEDLC e-tongue to distinguish multi-analytes was scrutinized. For this purpose, we discriminated basic tastes at a concentration below human threshold. Aqueous solutions with NaCl (salty), HCl (sour), caffeine (bitter), and sucrose (sweet) 0.1 mmol L^{-1} were prepared. Sweetness impacts on prompting nutrient sources and bitterness prevents the ingestion of harmful substances, whereas sourness is found in organic acids and saltiness is related to ions that act as markers of the electrolyte balance status.[5] Based on **Figure S3A,B**, the C_d vs. frequency plots were in accordance with the increasing conductivity (AJ Micronal AJX-522, São Paulo, Brazil) of the basic taste solutions. As verified throughout this work, these spectra exhibited the same profile and the C_d plots were distinct on each other especially in the frequencies lower than 10^2 Hz, where the charging of EDL governs the capacitance.

The responses were reproducible and depended on the sample nature. The patterns were then analyzed by PCA that projected the multivariate signals in a training matrix. The C_d vs. potential spectra are demonstrated in **Figure S3C**. As expected, the signals of C_d were distinct on each other in both magnitude and profile. The potential-based signals provided an efficient means to distinguish the solutions. The frequency-based clustering map in **Figure S3D** presents the PCA score plots. Each point means the global response pattern for an

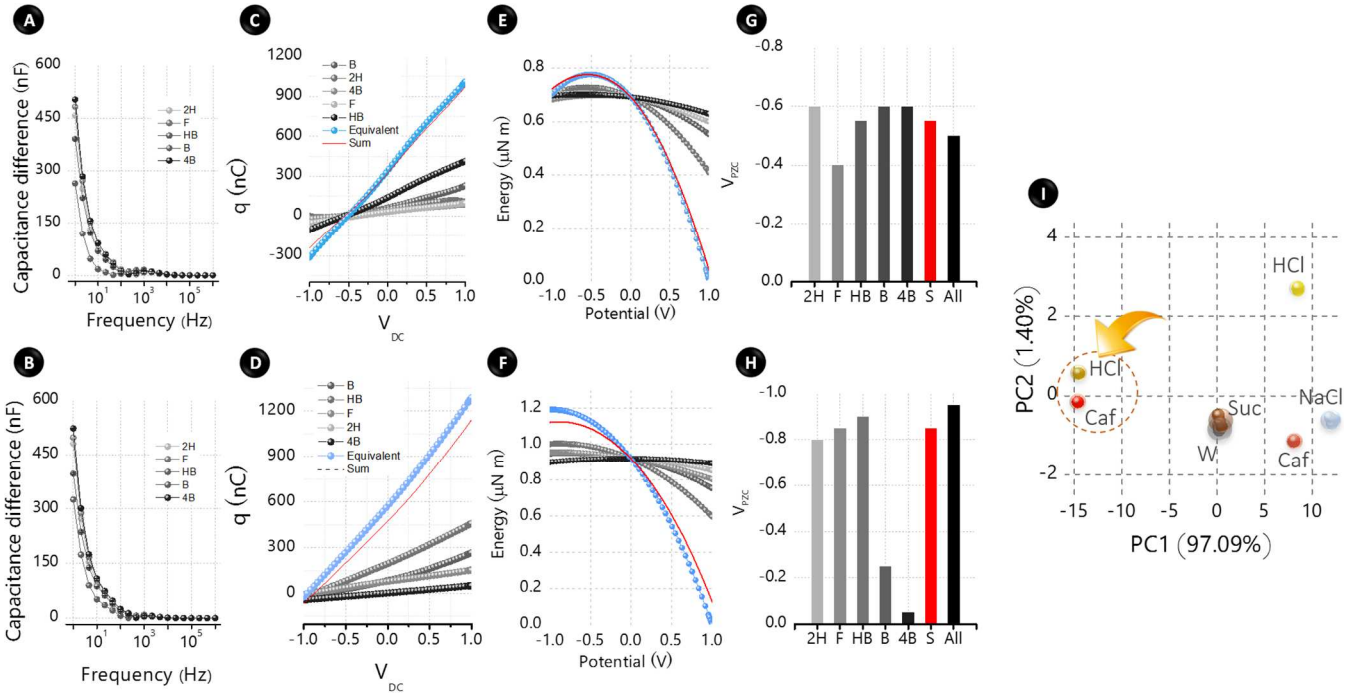

Figure S2. Capacitance differences in relation to water data **(A,B)**, charge plots **(C,D)**, electrocapillary curves **(E,F)**, and V_{PZC} **(G,H)** for solutions of HCl and of caffeine at 0.1 mmol L^{-1}, respectively. **(I)** PCA score plots of flavours (0.1 mmol L^{-1}) considering potential-based fingerprints. The plots in **(C,D)** and **(E,F)** were calculated from simple and double integrals of the potential plots in **Figure 2(C,D)** (main text), respectively. In **(I)**, the yellow arrow indicates the data obtained from responses independently recorded by the five graphite cores.

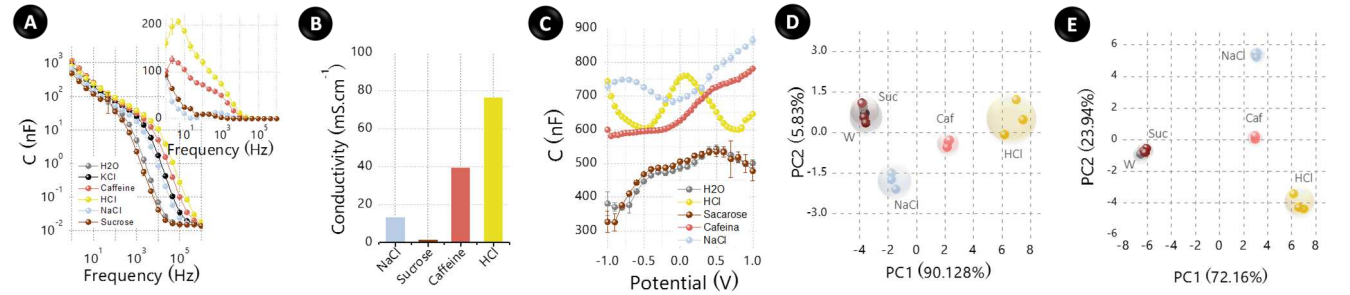

Figure S3. Discrimination of basic taste solutions at 0.1 mmol L^{-1}. **(A)** Spectra of C_d *vs.* frequency, **(B)** conductivities of the solutions, **(C)** plots of C_d *vs.* potential, and PCA score plots from **(D)** frequency-based fingerprints and **(E)** both the response patterns (spectra of C_d *vs.* frequency and *vs.* potential). Inset in **(A)** presents capacitance differences in relation to water data.

individual sample attained by the sensor. The basic tastes were recognized in clusters with no overlap despite the moderate data dispersion. While reasonable and strong classifications present S of 0.51 to 0.70 and 0.71 to 1.00, respectively, this parameter was 0.86 that means a clear data separation.[1c] When compared with C_d vs. frequency plots, the C_d vs. potential spectra produced lower deviations as it can be seen in the PCA plots of **Figure 3A** (main text). This feature led to an improvement on S that was determined as 0.98. This parameter was 0.94 by the combined use of the two previous spectra as response patterns, which produced the clustering map in **Figure S3E**.

Aqueous solutions of NaCl and HCl at different concentrations were measured to examine whether the pattern sensor can respond to the analytes in a dose-dependent mode. A positive correlation between C_d and analyte amount (0.1 to 1.0 mmol L^{-1}) was observed as shown in **Figure S4A-D**. This data is because of the raise in the number of charge carriers and EDL narrowing, which produces a nonlinear increase in the rate for accumulating excess charge density per 1 V.[2] Considering the response patterns based on frequency and potential, the PCA score plots in **Figure S4E,F** revealed tight clusters. S was 0.86 for both NaCl and HCl. Since the PC2 values were lower than 3%, only the PC1 data were used to obtain analytical curves as portrayed in **Figure S4G,H**. The data fitting with larger determination coefficients ($R^2 > 0.9$) obeyed the Freundlich[5] model as discussed in the main text.

6. Discrimination of mixture solutions

Solutions with sucrose and HCl as well as caffeine and NaCl at distinct concentrations were successfully analyzed proving that the e-tongue is able to provide multielement detection from a single test assembly. Solutions of these analytes (0.1 mmol L^{-1}) were mixed at the v/v ratios of 0%, 20%, 40%, 60%, 80%, and 100%. The C_d plots are shown in **Figure 3B** (main text) and **Figure S5A-C**. From both the maps based on frequency and potential, the samples were clearly recognized in the PCA score plots of **Figure 3C** (main text) (0.96 S) and **Figure**

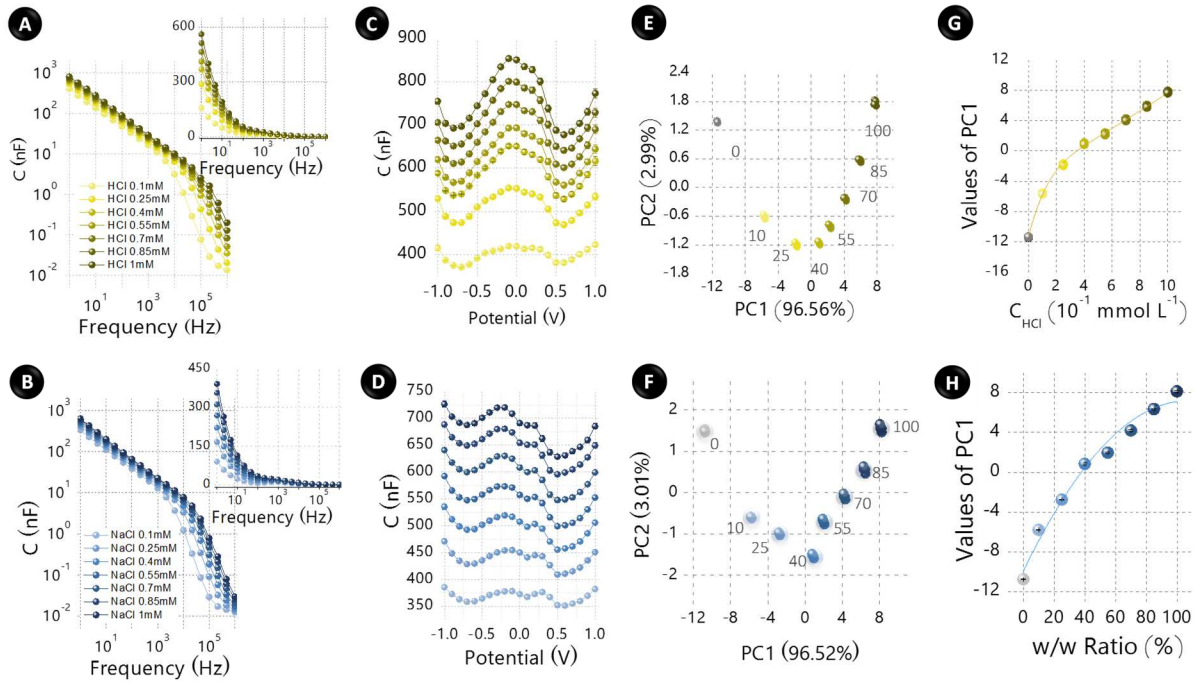

Figure S4. Discrimination of aqueous solutions of HCl and NaCl at different concentrations. **(A,B)** Spectra of C_d *vs.* frequency, **(C,D)** plots of C_d *vs.* potential, **(E,F)** PCA plots from both the patterns (spectra of C_d *vs.* frequency and *vs.* potential), and **(G,H)** analytical curves for HCl and NaCl, respectively. Insets in **(A,B)** present C_d differences in relation to water data.

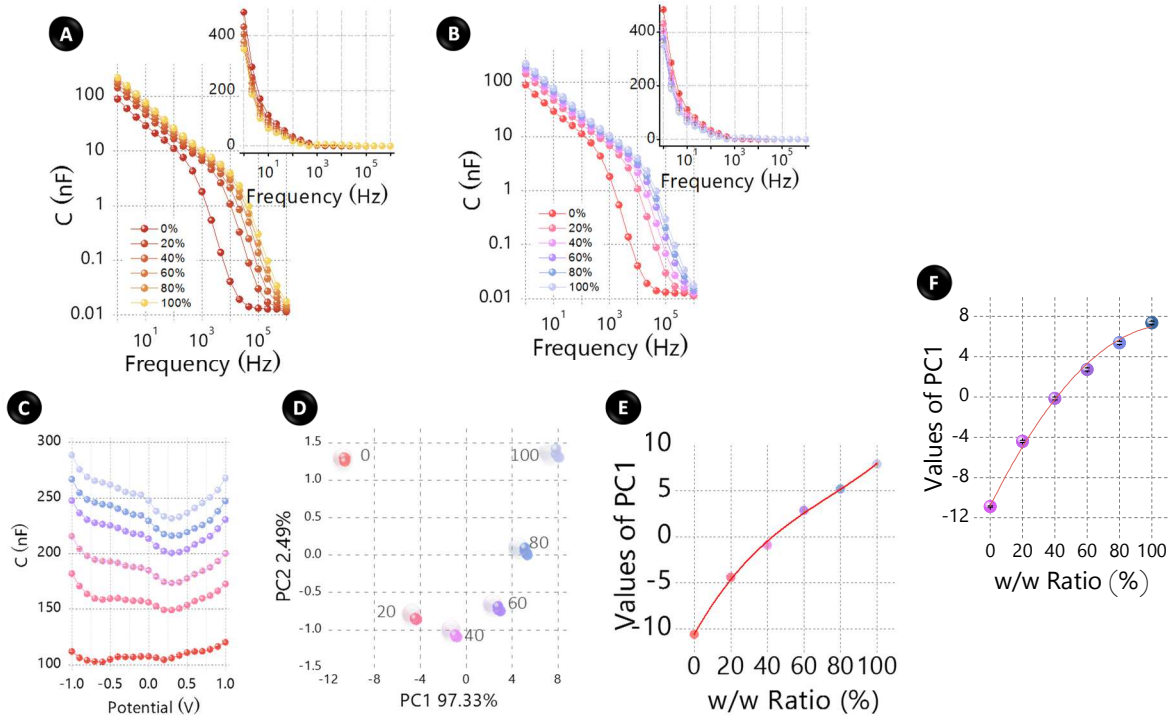

Figure S5. Discrimination of mixture solutions of sucrose-HCl and caffeine-NaCl at different concentrations. Spectra of C_d *vs.* frequency for **(A)** sucrose-HCl and **(B)** caffeine-NaCl, **(C)** plots of C_d *vs.* potential, **(D)** PCA score plots from both the patterns (spectra of C_d *vs.* frequency and *vs.* potential), and **(E)** analytical curve for caffeine-NaCl. **(F)** Analytical curve for sucrose-HCl. Insets in **(A,B)** present capacitance differences in relation to water data.

S5D (0.97 S). All the points were properly arranged in isolated clusters in consistence with a realistic situation. The data distribution of the mixtures also followed the Freundlich model as shown in **Figure S5E,F** ($R^2 > 0.9$). Approximately 97% and 3% of response variance were explained by PC1 and PC2, respectively. Hence, the analytical curves were once again based on PC1 only. These results demonstrate a potential ability of the µEDLC to discriminate samples with complex composition. In the previous analyses, positive correlations between C_d and analyte amount were verified in accordance with Freundlich model for PC1-based analytical curves as follows:[6]

$$C_d = K_a C^{1/n} \quad (5)$$

Where K_a is an adsorption constant, C is the concentration of the analyte, and $1/n$ is a heterogeneity factor. Thus, in addition to the PZCs, this fitting further supports the specific adsorption of anions on probe/solution interfaces.

In the previous applications, analyses for KCl 0.1 mmol L^{-1} in water were also realized after sample to ascertain both the sensor repeatability and the possible electrode contamination. The data showed low dispersion, thus indicating high repeatability and absence of contamination of the probes. The reason for this data is the high chemical stability and inertia of carbon as it is well known.[7]

7. Discrimination of metal ions

We investigated five samples of a brand of mineral water incorporating spiked ions (Ni^{2+}, Co^{2+}, Cd^{2+}, Al^{3+}, and Fe^{3+}). The selected species are customarily found in this type of sample at a wide range of concentrations. In this assay, the metal ions were prepared at 0.1 mmol L^{-1} (an average value) to avoid the effect of concentration on response patterns. From the spectra of C_d as a function of frequency and, in special, potential in **Figure S6A,B**, respectively, the plots of PCA demonstrated the sensor is also able to differentially interact with the cations. Weak discrimination of these species was achieved from the frequency-based patterns (0.48 S) as depicted in PCA plots of **Figure S6C**. Otherwise, the C_d vs. potential plots led to a strong recognition of the samples according to plots of PCA in **Figure S6D** (0.82 S). This sensing performance was not improved by the use of both fingerprints, from which the solutions were only reasonably classified (0.69 S). In addition to nature and extent of the adsorptions on EDL, the cross-reactive C_d data can be also linked to the distinct hydrolysis extents of the cations, with specific variations on pH values.

8. Discrimination of water samples

We checked the practical potential of the e-tongue in the identification of different types of drinking water, namely, five brands of commercial mineral water, tap, lake (obtained in the city of Campinas-SP, Brazil), filtered, and distilled water. The pattern sensors meet the requirements of discriminating a plenty of ions in mixtures[8] and, then performing the quality control of drinking water that is of paramount relevance towards human health. The metal ions are nonbiodegradable and highly soluble in water, bringing human health problems by damaging the central nervous system, liver, kidney, bone, and teeth. These metals can also act like carcinogen, mutagen, and teratogen agents.[8a,8c] The C_d plots as a function of frequency and potential in **Figure S7A,B** afforded the recognition of the water samples as shown in PCA plots of **Figure 3D** (main text). Since the proximity between the data points reflects the chemical similarity of the samples, the distribution of all the clusters was in agreement with the media conductivities in **Table S1** as expected.

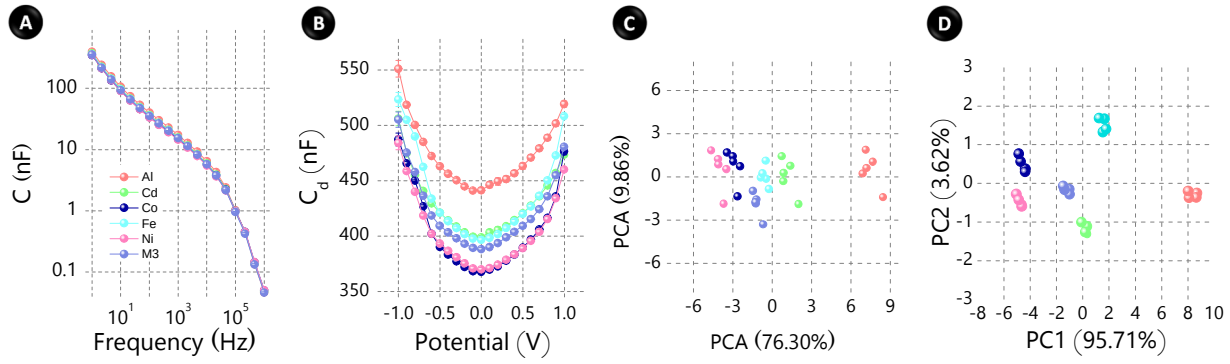

Figure S6. Spectra of C_d **(A)** *vs.* frequency and **(B)** *vs.* potential for a brand of commercial mineral water containing spiked ions (Ni^{2+}, Co^{2+}, Cd^{2+}, Al^{3+}, and Fe^{3+}) at 0.1 mmol L^{-1}. PCA score plots from **(C)** plots of C_d *vs.* frequency and **(D)** both the response patterns.

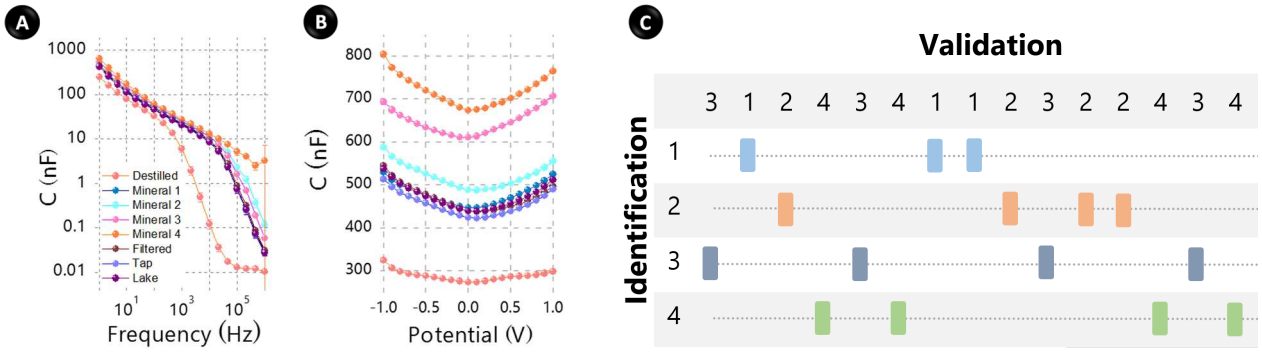

Figure S7. Spectra of C_d **(A)** *vs.* frequency and **(B)** *vs.* potential for the drinking water samples. **(C)** Accuracy of the recognition of 15 unknown samples.

Table S1. Conductivities of the investigated water samples

Samples	Distilled	Mineral 1	Mineral 2	Mineral 3	Mineral 4	Mineral 5	Filtered	Tap	Lake
Conductivity (μS cm^{-1})	5.4	140.35	335.0	187.2	601	128.5	117.7	196.3	85.5

We further checked the robustness of the e-tongue through the identification of 15 unknown samples that were randomly selected from 4 brands of mineral water as shown in **Figure S7C**. For application in the real world, the response patterns of standard samples (training set) are recorded and, then stored in a computer database. Afterwards, unknown samples (validation set) can be identified in a simple way by directly matching the patterns. Herein, the discrimination accuracy percentage of the 15 unknown samples was 100%.

9. Recognition in the presence of nanotubes

Considering the C_d plots (as a function of both frequency and potential) recorded for the nine drinking water samples soon after their stirring-assisted incubation (without nanomaterial sedimentation), the PCA graphic revealed a just reasonable separation of the data points (0.76 S). Nonetheless, a notorious improvement on pattern classification was noted when analyzing the supernatant samples after interaction with multi-walled carbon nanotubes (MWCNTs) according to the PCA plots in **Figure 3F** (main text) S (0.92 S). In addition to S, other data that shows the improvement on classification ability is associated with the increase in the dimensionality of the PCA clusters. Regarding the results for untreated samples, PC2 raised from 4% to 17% representing a higher distribution of the total variance in two dimensions.

In practice, 200 μL of dispersion bearing MWCNTs 500.0 ppm to water were dipped into 800 μL of sample. An incubation time of 10 min was then needed. Next, the dispersion was kept at rest for 30 min for aggregate sedimentation. Only the supernatant was collected and introduced in the microfluidic device to get the two spectra of C_d. Typical e-tongues would be based on MWCNTs with distinct oxidation extents. In contrast, we used only one type of nanotube (oxidized for 48 h) due to the existence of other diverse signal diversification factors, associated with the graphite cores.

For oxidation, the MWCNTs were dispersed in HNO_3 9.0 mmol L^{-1} at 5:1 ratio (mg of MWCNT to mL of HNO_3) using ultrasound bath during 5 min. Following, the dispersion was magnetically stirred at 150 °C in a conventional reflux system for MWCNT oxidation. The oxidation time was 48 h. Next, the nanotubes were washed with deionized water until pH 6 utilizing Millipore filtration and membrane of polytetrafluoroethylene (0.2 μm). Finally, the MWCNTs were lyophilized, dispersed in water ultrasound bath for 1 h, and then stored at room temperature. Images of the nanotubes were obtained by FE-SEM (FEI Quanta-450, Hillsboro, OR) and transmission electron microscopy (TEM, JEOL TEM-MSC LaB_6 2100, Peabody, MA). The latter analyses were made with an acceleration voltage of 200 kV. The samples were prepared by drying the MWCNTs in air flow on carbon-coated copper grid (ultrathin carbon/holey carbon, 400 mesh copper grid). The images were acquired on a single-tilt sample holder using Gatan MSC798 TV camera, Gatan Digital Micrograph, and EMMENU programs. **Figure S8A** presents SEM images of the oxidized MWCNT surfaces.

Measurements by inductively coupled plasma-atomic emission spectrometry (ICP-AES) confirmed the interactive character of the cation adsorption by the nanotubes. These analyses were performed by Perkim Elmer Optima 8000 dual view equipment (Waltham, MA) as experimental conditions in **Table S2**. The corresponding results in **Figure S8B** present the concentration drop ratios of a plenty of metal ions in a supernatant sample compared with the initial sample. From these specific ratios, we can state the interactions depend on nature of the cations.

New possibilities are generated towards pattern sensors from this work. Alternatively, as stated in the main text, the heterogeneity of the cores may be used to get e-tongues from a single probe owing to cross-interactions with distinct regions of the core. In addition, while the C_d vs. potential fingerprints and colloidal stability-based strategy with oxidized MWCNTs can be used by any capacitive approach, further extensions of the present platform may be envisaged for improving the recognition ability. Options include the recording of the C_d *vs.* potential plots in other frequencies such as intermediate values driven by C_M and the raise in the number of probes. As aforesaid, our

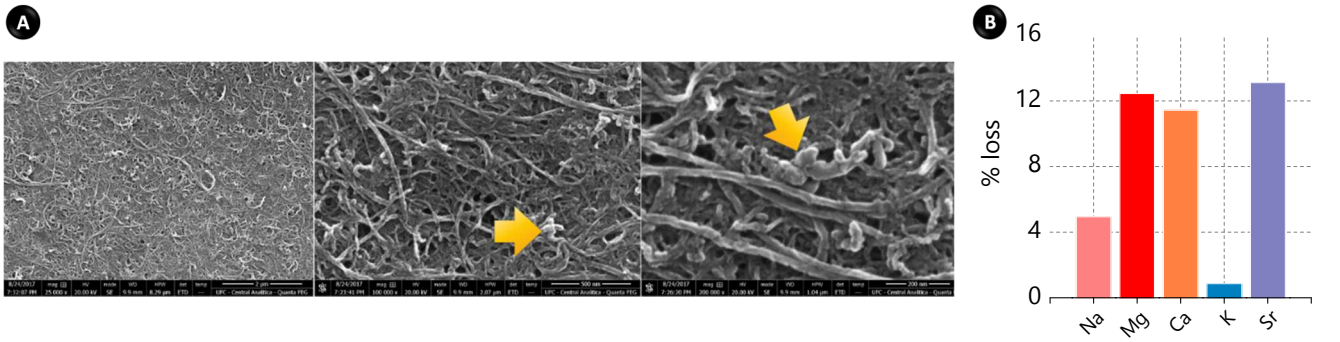

Figure S8. (A) SEM images of the oxidized MWCNT. **(B)** Concentration drop ratios of metal ions in a supernatant sample (M4 according to **Table S1** and caption of **Figure 3** in main text) compared with the initial sample. In **(A)**, the yellow arrows portray formed debris.

Table S2. Experimental conditions of the ICP-AES measurements

Parameter	Conditions
Generator Radio Frequency (MHz)	40
Power (watts)	1500 (S), 1350 (Ba) and 1400 (other ions)
Plasma gas flow rate (L min^{-1})	8 (S, Ca, Ba) and 10 (other ions)
Auxiliary gas flow rate (L min^{-1})	0.5
Nebulization gas flow rate (L min^{-1})	0.45
Observation height (mm)	15.0
Inner diameter of the central tube (mm)	2.0
Nebulization camera	Cyclonic
Nebulizer	Meinhard Type K1

sensor guarantees cross-reactive tests from a single scan regardless of the number of sensing probes. Notwithstanding the significance of the chemically modified sensing probes in pattern applications, we believe the use of ready-to-use probes can be extended to other targets and matrices to afford a quick screening in mass-production and/or day-to-day analysis situations.

10. References

1. a) C. L. Camargo, L. S. Shiroma, G. F. Giordano, A. L. Gobbi, L. C. S. Vieira and R. S. Lima, *Anal. Chim. Acta* 2016, **940**, 73–83; b) C. A. Teixeira, G. F. Giordano, M. B. Beltrame, L. C. S. Vieira, A. L. Gobbi and R. S. Lima, *Anal. Chem.* 2016, **88**, 11199–11206; c) F. M. Shimizu, F. R. Todao, A. L. Gobbi, O. N. Oliveira, Jr., C. D. Garcia and R. S. Lima, *ACS Sens.* 2017, **2**, 1027–1034; d) F. M. Shimizu, A. M. Pasqualeti, F. R. Todão, J. F. A. de Oliveira, L. C. S. Vieira, S. P. C. Gonçalves, G. H. da Silva, M. B. Cardoso, A. L. Gobbi, D. S. T. Martinez, O. N. Oliveira, Jr. and R. S. Lima, *ACS Sens.* 2018, **3**, 716–726; e) G. F. Giordano, C. L. Camargo, L. C. S. Vieira, M. A. d'Ávila, B. C. Couto, R. M. de Carvalho, A. L. Gobbi and R. S. Lima, *Energy Fuels* 2018, **32**, 6577–6583; f) G. F. Giordano, L. C. S. Vieira, A. L. Gobbi, L. T. Kubota and R. S. Lima, *Anal. Chim. Acta* 2018, **1033**, 128–136; g) D. H. Martucci, F. R. Todão, F. M. Shimizu, T. M Fukudome, S. F. Schwarz, E. Carrilho, A. L. Gobbi, O. N. Oliveira Jr. and R. S. Lima, *Electrochim. Acta* 2018, **292**, 125–135; h) R. A. G. de Oliveira, C. Y. N. Nicoliche, A. M. Pasqualeti, F. M. Shimizu, I. R. Ribeiro, M. E. Melendez, A. L. Carvalho, A. L. Gobbi, R. C. Faria and R. S. Lima, *Anal. Chem.* 2018, **90**, 12377–12384.
2. R. N. Bhowmik, *Compos. Part B-Eng.* 2012, **43**, 503–509.
3. a) J. O'M. Bockris, A. K. N. Reddy and M. Gamboa-Aldeco, *Modern Electrochemistry: Fundamentals of Electrodics 2A*, *Vol. 2,* 2nd ed., Kluwer Academic Publishers, New York, 2002, pp. 806–919; b) A. L. Bard and L. R. Faulkner, *Electrochemical Methods: Fundamentals and Applications*, 2nd ed., John Wiley & Sons, New York, 2001, pp. 368–534.
4. a) V. Lockett, R. Sedev, J. Ralston, M. Horne and T. Rodopoulos *J. Phys. Chem. C* 2008, **112**, 7486–7495; b) H. Ji, X. Zhao, Z. Qiao, J Jung, Y. Zhu, Y. Lu, L. L. Zang, A. H. MacDonald and R. S. Ruoff, *Nature communications* 2014, **5**, 3317.
5. L. Lu, X. Hu and Z. Zhu, *Trends Analyt. Chem.* 2017, **87**, 58–70.
6. A. C. Soares, J. C. Soares, V. C. Rodrigues, H. D. M. Follmann, L. M. R. B. Arantes, A. C. Carvalho, M. E. Melendez, J. H. T. G. Fregnani, R. M. Reis, A. L. Carvalho and O. N. Oliveira, Jr., *ACS Appl. Mater. Interfaces* 2018, **10**, 36757–36763.
7. Y. Yu, P. C. Joshi, J. Wu and A. Hu, *ACS Appl. Mater. Interfaces* 2018, **10**, 34005–34012.
8. a) X. Zhou, J. Nie and B. Du, *ACS Appl. Mater. Interfaces* 2017, **9**, 20913–20921; b) L. Zhang, X. Huang, Y. Cao, Y. Xin and L. Ding, *ACS Sens.* 2017, **12**, 1821–1830; c) W. He, L. Luo, Q. Liu and Z. Chen, *Anal. Chem.* 2018, **90**, 4770–4775; d) S.-F. Xue, Z.-H. Chen, X.-Y. Han, Z.-Y. Lin, Q.-X. Wang, M. Zhang and G. Shi, *Anal. Chem.* 2018, **90**, 3443–3451.